Linear scaling algorithm of real-space density functional theory of electrons with correlated overlapping domains

Nobuko Ohba[a,b], Shuji Ogata[a,*], Takahisa Kouno[a,c], Tomoyuki Tamura[a], Ryo Kobayashi[a]

[a] *Graduate School of Engineering, Nagoya Institute of Technology, Nagoya 466-8555, Japan*
[b] *Toyota Central Research & Development Laboratories, Inc., Nagakute, Aichi 480-1192, Japan*
[c] *Institute for Solid State Physics, The University of Tokyo, Kashiwa 277-8581, Japan*

Abstract

The real-space grid based implementation of the Kohn-Sham density-functional theory of electrons using the finite difference method for derivatives of variables, has attractive features of parallelizability and applicability to various boundary conditions in addition to universality in target materials. Following the divide-and-conquer strategy, we propose a linear scaling algorithm of it by advancing the algorithm in [Shimojo et al, Comput. Phys. Comm. 167 (2005) 151]. In the Kohn-Sham-type equation for a domain, we introduce (i) the density-template potential for density continuity with simple stepwise weight-functions and (ii) the embedding potential to take into account all the quantum correlation effects with other overlapping domains in addition to the classical effects of ionic and electronic Coulomb potentials. We thereby realize reasonably high accuracies in atomic forces with relatively small numbers of buffer ions irrespective of the electronic characters of materials. The timing tests on parallel machines demonstrate the linear scaling of the code with little communication time between the domains.

Keywords: linear scaling algorithm, real-space implementation, density functional theory, divide-and-conquer, electronic structure, embedding effect

*Corresponding author
Email address: ogata@nitech.ac.jp (Shuji Ogata)

1. Introduction

The Kohn-Sham (KS) formulation of the density-functional theory (DFT) [1, 2], which uses the electron density instead of $3N$-dimensional wavefunction (the number of electrons N) as the basic variable, has made great successes in analyzing the ground state electronic properties of small systems [3]. Recent advancement in fabricating electronic devices and systems [4] at the nano-meter scale such as the LSI and micro-electromechanical systems [5] motivates us to apply the KS-DFT scheme to such complex-structured systems. Issues of interest include: prediction of microscopic structures of materials interfaces and their strengths, and understanding reaction dynamics in both fabrication and failure processes [6, 7]. Among various forms of the numerical implementation of the KS-DFT scheme, it is conventional to use planewaves [8, 9, 10] to represent electronic orbitals of a supercell of a solid-state system under the periodic boundary conditions (PBC's). The merits of using the basis set of the planewaves include: their independence on ionic positions, high accuracy in the computation of the kinetic energy, efficient usage of the Fast Fourier Transform (FFT) [11] method, and universality in target materials. Using such a delocalized basis set as the planewaves, however, make the conventional KS-DFT code too slow even on parallel machines to be applied directly to such a large system.

One of the promising methods to calculate the static and dynamic properties of such an inherently multi-scaled system with the KS-DFT scheme is to use the hybrid quantum-classical (QM-CL) method [12]. In the hybrid method, we apply, for instance, the KS-DFT scheme to a relatively small region selected adaptively, while the classical inter-atomic potential to the environmental region [13, 14]. The mechanical coupling of the two regions at the atomistic scale is realized by introducing virtual buffer atoms to both descriptions [15]. The atomic forces in both QM and CL regions are calculated concurrently to simulate the dynamics of atoms. At the re-selection of the QM region, the calculated atomic forces are unchanged practically, while the energy of the system is not.

The real-space grid (RG) based KS-DFT method [16, 17, 18, 19, 20, 21, 22, 23] has been used for the QM calculation in the hybrid QM-CL method, in which the eigen orbitals and the potentials are represented on a set of grid points in 3D and their derivatives are evaluated by the finite difference

method. The RGDFT method has the same computation scale-order and universality in target systems as the conventional planewave-based KS-DFT method does. Furthermore the RGDFT method is applicable to charged systems with various boundary conditions including external electric field. As the RGDFT method does not use the FFT method that is not suited to parallel machines, it is highly parallelizable by spatial decomposition of the grid points [21, 23]. Former applications of the hybrid QM-CL method include: calculation of the migration energy of an O atom in stressed Si [24], simulation of the Li diffusion in stressed graphite [25], and pressure-induced oxidation dynamics at the contact area of diamond tip and Si surface in moisture environment [26]. The larger QM region, the better from the viewpoint of the physical accuracy. On the other hand, the QM computation at every time step should be finished within reasonable timings. Balancing the two needs, we set the QM regions composed of about 100 atoms only (about 200 atoms including the buffer atoms) in the former hybrid QM-CL simulation runs [24, 25, 26, 27].

The atomic orbital (AO)-based KS-DFT method [28, 29], in which eigen orbitals are represented by a localized basis set of electronic orbitals of free atoms or their modifications, can also be used in the hybrid QM-CL method. However, careful choice of the basis set is essential for high accuracy, particularly for metallic systems or when chemical bonds break. Despite such inconvenience, the AODFT method has been widely used for various molecules because of its high computation speed and accumulation of experiences. Its extension to the order-N scheme has been proposed following the divide-and-conquer (DC) strategy [30, 31, 32, 33, 34, 35]. In such a DC-AODFT method, a target system is divided into overlapping domains with buffer ions. For each domain, the eigen orbitals represented by the AO basis set are obtained as the self-consistent eigen functions of the total KS equation up to the global Fermi energy. The total density is then obtained as the summation of the weighted densities of the domains.

The RGDFT method has the attractive feature of universality in target materials and settings resulting from no usage of the AO to represent the eigen orbitals. With application to a large QM region in the hybrid QM-CL simulation in mind, we will therefore develop an order-N RGDFT method following the DC strategy. Since no basis set will be used in the DC-RGDFT, the electronic states relating to the buffer ions may vary significantly depending on the effective potential field created by other domains. Controlling those electronic states relating to the buffer ions to resemble the

states in the original system will be crucial for the DC-RGDFT method to give accurate density and atomic forces. Such a control has not been considered in the DC-AODFT method because of the limited flexibility of the AO-based orbitals.

A seminal paper [36] exists for such a DC-RGDFT scheme. Possibility of applying the DC-RGDFT scheme to large-scale systems were demonstrated using massively parallel machines [37, 38]. In the formulation in Ref. [36], the embedding effect of the electronic kinetic energy for a domain was considered in addition to that of the electronic and ionic Coulomb potentials. Unfortunately, the formulas were sensitive to the forms of the weight functions that were introduced to divide the total system into the domains. The quantum embedding effect of the exchange-correlation potential was ignored. Critical analyses on the accuracy of atomic forces have not been shown. Considering these, in the present paper, we will include all the embedding effects of the electronic and ionic Coulomb potentials and of electronic kinetic and exchange-correlation potentials through formulas that are not sensitive to the weight functions. Therefore a proper embedding potential will be introduced to the KS-type equation for a domain. In addition, we will introduce a novel density-template potential for the overlapping area of the domains to the KS-type equation to realize continuation of density. We will demonstrate that the combination of the embedding and density-template potentials gives accurate atomic forces for various materials as ceramics, semiconductors, and metals with relatively small numbers of buffer ions. Benchmark tests of the DC-RGDFT code on parallel machines will be performed to show its order-N scaling and practical computation times for large-scale atomic clusters.

Organization of the rest of the this paper is the following. In §2, based on the RGDFT method, present formulation of the DC-RGDFT method will be explained. In §3, physical accuracies of both density and atomic forces for various materials will be analyzed. Computation times of the DC-RGDFT code on parallel machines will be presented. Summary and concluding remarks will be given in §4.

2. Methods

2.1. Real-space implemented Kohn-Sham DFT (RGDFT) method

In this subsection we summarize the RGDFT method [16, 17, 18, 19, 20, 21, 22, 23] before we advance it to the DC-type. Let us consider an atomic cluster composed of $N_{\rm ion}$ ions with charge numbers $\{Z_i\}$ at positions

$\{\vec{R}_i\}$ $(i = 1, 2, ..., N_{\rm ion})$ and the valance electrons. For simplicity, the charge-neutral system is assumed though the formulation is applicable to non-neutral systems also; the total number of electrons $N_e = \sum_i Z_i$.

The well-known Kohn-Sham equation for the eigen orbital $\phi_n(\vec{r})$ with the eigen energy ϵ_n is

$$\left[-\frac{1}{2}\nabla^2 + v_{\rm H}(\vec{r}) + \sum_{i=1}^{N_{\rm ion}} v_{{\rm ion},i}(\vec{r}) + v_{\rm xc}(\vec{r})\right]\phi_n(\vec{r}) = \epsilon_n\phi_n(\vec{r}) \tag{1}$$

in the atomic unit (i.e., $m_e = \hbar = e = 1$). The Hartree potential in Eq. (1) is

$$v_{\rm H}(\vec{r}) = \int d\vec{r'}\frac{\rho(\vec{r'})}{|\vec{r} - \vec{r'}|} \tag{2}$$

or

$$\nabla^2 v_{\rm H}(\vec{r}) = -4\pi\rho(\vec{r}) \tag{3}$$

with the density of electrons

$$\rho(\vec{r}) = \sum_{n=1}^{N_e/2} 2|\phi_n(\vec{r})|^2 \tag{4}$$

in the spin neutral case.

The pseudopotential of ion-i, $v_{{\rm ion},i}(\vec{r})$, for $\phi_n(\vec{r})$ acts as

$$v_{{\rm ion},i}(\vec{r})\phi_n(\vec{r}) = v_{{\rm L},i}(\vec{r})\phi_n(\vec{r}) + v_{{\rm NL},i}(\vec{r})|\phi_n\rangle \tag{5}$$

with

$$v_{{\rm NL},i}(\vec{r})|\phi_n\rangle = \sum_{l=0}^{l_{\rm max}}\sum_{m=-l}^{l}\frac{\phi^{\rm ps}_{lm,i}(\vec{r})\Delta v_{l,i}(\vec{r})\int d\vec{r'}\phi^{\rm ps*}_{lm,i}(\vec{r'})\Delta v_{l,i}(\vec{r'})\phi_n(\vec{r'})}{\int d\vec{r}\phi^{\rm ps*}_{lm,i}(\vec{r})\Delta v_{l,i}(\vec{r})\phi^{\rm ps}_{lm,i}(\vec{r})}\ . \tag{6}$$

Here the Kleinman-Bylander form [39] is adopted for the treatment of the non-local pseudopotential. The norm-conserving pseudopotentials [40] are used. The $\phi^{\rm ps}_{lm,i}(\vec{r})$ in Eq. (6) is the pseudo eigen-orbital for a free atom-i at angular state (l, m). The pseudopotential at a chosen angular state $l = l_{\rm loc}$ (often the maximum of l) is regarded as the local pseudopotential, and the deviation of the pseudopotential from the local one as the non-local pseudopotential:

$$v_{{\rm L},i}(\vec{r}) \equiv v_{l_{\rm loc},i}(\vec{r}) \ \text{ and } \ \Delta v_{l,i}(\vec{r}) \equiv v_{l,i}(\vec{r}) - v_{l_{\rm loc},i}(\vec{r}) \tag{7}$$

with the pseudopotential $v_{l,i}(\vec{r})$ for a free ion-i at angular state l. The $v_{\mathrm{L},i}(\vec{r})$ contains the long-ranged Coulomb potential, while the $\Delta v_{l,i}(\vec{r})$ is short-ranged.

The $v_{\mathrm{xc}}(\vec{r})$ in Eq. (1) is the exchange-correlation potential defined as the functional derivative of the exchange-correlation energy:

$$v_{\mathrm{xc}}(\vec{r}) = \frac{\delta E_{\mathrm{xc}}(\rho)}{\delta \rho(\vec{r})} \ . \tag{8}$$

Various approximation formulas of $E_{\mathrm{xc}}(\rho)$ are given in literatures. For simplicity, we use the local density approximation (LDA) formula in Ref. [41].

The eigen orbitals in Eq. (1) are solved numerically through the self-consistent field (SCF) iteration [8, 9, 42] under the orthonormalization constraint:

$$\int d\vec{r} \phi_i^*(\vec{r}) \phi_j(\vec{r}) = \delta_{i,j} \equiv \begin{cases} 1, & \text{for } i = j \ , \\ 0, & \text{for } i \neq j \ . \end{cases} \tag{9}$$

The number of SCF iterations required to reach the convergence, which is independent of the target system size, is typically twenty. In the conventional planewave-based KS-DFT method, eigen orbitals are represented using the planewaves under the PBC's. And the SCF iteration procedure contains the local iteration for all the energy levels considered. In sweeping the orbitals for a given $\rho(\vec{r})$ in the local iteration procedure, orbitals are updated one by one from the lowest to highest energy levels by the conjugate gradient method with the Gram-Schmidt orthonormalization [11] to the orbitals at lower energy levels.

In the RGDFT method, we set the Cartesian grid points in 3D with the grid size h to describe the eigen orbitals and the potentials. The grid size h in unit of the Bohr radius $a_{\mathrm{B}} \approx 0.529$ Å corresponds to the cutoff energy $0.5(\pi/h)^2$ (a.u.) (1 a.u. of energy ≈ 27.2 eV) in the conventional planewave-based KS-DFT method. The overall shape of the grid points is spherical with radius $r_{\max}$, which is determined to enclose all the ions with a few Å vacuum width so that $\rho(\vec{r}) = 0$ at $r = r_{\max}$. The second derivative operations in the three directions in the KS and Poisson equations are calculated by the high-order (fourth or more) finite difference method [11, 16, 22, 23] using the data on multiple grid points in both plus and minus sides. For the ion with relatively deep pseudopotential as oxygen, a smaller grid size of $h/3$ is used at around the ion only to represent the pseudopotential accurately [43]. The RGDFT method is well suited to the parallel computation environment. It

is free from the FFT method that becomes inefficient for massively parallel machines. The idea of spatial decomposition of the grid points works well for parallel machines. In addition, the RGDFT method has a unique feature of numerical stability that helps to realize high computation performance of the Gram-Schmidt orthonormalization of the orbitals as explained below. While the Gram-Schmidt orthonormalization needs to be performed orbital-by-orbital for stability reasons in the conventional planewave-based method, it can be performed for all the orbitals together in the RGDFT method after the orbital sweep in the local iteration procedure [23]. That rearrangement of the Gram-Schmidt orthonormalization procedure improves the computation performance [23] on a parallel machine by employing a highly tuned linear-algebra library.

2.2. Divide-and-conquer-type RGDFT method

For the present formulation, we divide a target system into the total of $N_{\rm d}$ *basic domains* arranged in 3D, as depicted in Fig. 1(a) for 2D case. The boundary surface between the neighboring basic-domains are denoted as $\vec{S}_{\rm bdry}$. To each basic domain, we add a surface layer taken from the neighboring basic-domains with the cutoff depth $d_{\rm c}$ from $\vec{S}_{\rm bdry}$ to define the *domain* that overlaps with neighboring domains. For a domain, we call those ions located in the basic domain as the *real* ions as depicted in Fig. 1(b). Those ions located in the additional surface layer are called the *buffer* ions. Other ions that are neither real nor buffer are the *external* ions. The Coulomb potential due to the external ion should be considered in the domain, while it will be modified at the vicinity of the ion so that the valence electrons become unbound to it. The weight function $W_I(\vec{r})$ for domain-I should obey the sum rule of $\sum_{I=0}^{N_{\rm d}-1} W_I(\vec{r}) = 1$ at any $\vec{r}$. For simplicity we assume the stepwise form for $W_I(\vec{r})$: that is, $W_I(\vec{r}) = 1$ in basic domain-I, while $W_I(\vec{r}) = 0$ outside the basic domain.

For domain-I, the density ρ_I(r) is obtained through the KS-type equation explained below with the Fermi energy common to all the domains. The grid points form a sphere of radius $r_{\rm max}$ with its center set at the averaged position of the real and buffer ions. The value of $r_{\rm max}$ is determined so that the real and buffer ions are enclosed with sufficient vacuum width so that $\rho_I(\vec{r}) = 0$ at $r = r_{\rm max}$. The total density defined as

$$\rho_{\rm tot}(\vec{r}) \equiv \sum_{I=0}^{N_d-1} W_I(\vec{r})\rho_I(\vec{r}) \tag{10}$$

is thereby calculated, which corresponds to $\rho(\vec{r})$ in the RGDFT method. We call $W_I(\vec{r})\rho_I(\vec{r})$ the *real density* and $[1 - W_I(\vec{r})]\rho_I(\vec{r})$ the *shadow density* of domain-I.

The KS-type equation in the DC-RGDFT method for domain-I is

$$\Bigg[-\frac{1}{2}\nabla^2 + v_{\rm H}^{\rm DC}(\vec{r}) + \sum_{i=1}^{N_{\rm ion}} v_{{\rm ion},i}^{\rm DC}(\vec{r}) + v_{\rm xc}^{\rm DC}(\vec{r}) \\ + \; w_{\rm DT}(\vec{r})v_{\rm DT}(\vec{r}) + (1 - w_{\rm DT}(\vec{r}))v_{\rm emb}(\vec{r})\Bigg]\phi_n(\vec{r}) = \epsilon_n\phi_n(\vec{r}) \; . \quad (11)$$

Here the kinetic energy term (i.e., the 2nd derivative term) is the same as in the standard KS equation [see, Eq. (1)]. The exchange-correlation potential is

$$v_{\rm xc}^{\rm DC}(\vec{r}) = \frac{\delta E_{\rm xc}(\rho_{\rm tot})}{\delta\rho_{\rm tot}(\vec{r})} \; . \quad (12)$$

The density $\rho_I(\vec{r})$ is calculated as

$$\rho_I(\vec{r}) = \sum_{n=1}^{N_{e,I}/2} 2|\phi_n(\vec{r})|^2 \quad (13)$$

with either integer or non-integer number of electrons $N_{e,I}$ for domain-I. The global Fermi level is determined so that the total number of electrons becomes $N_e = \sum_{I=0}^{N_{\rm d}-1} N_{e,I}$.

The Hartree potential in Eq. (11) is defined as

$$v_{\rm H}^{\rm DC}(\vec{r}) = \int d\vec{r'}\frac{\rho_{\rm tot}(\vec{r'})}{|\vec{r} - \vec{r'}|} \; . \quad (14)$$

It includes the embedding effect of the electronic Coulomb potential from other domains. Note that $v_{\rm H}^{\rm DC}(\vec{r})$ is felt by both real and shadow densities.

As for the pseudopotentials $\{v_{{\rm ion},i}^{\rm DC}(\vec{r})\}$ in Eq. (11), those terms relating to the real and buffer ions are the same as that in $v_{{\rm ion},i}(\vec{r})$ in Eq. (1). On the other hand, the $v_{{\rm ion},i}^{\rm DC}(\vec{r})$'s relating to the external ions are modified at small r so that no bound orbital exists on them. That is, while a relatively short cutoff radius $r_{\rm L}^{\rm c}$ is used to calculate the local pseudopotential $v_{{\rm L},i}(\vec{r})$ of an external ion at $\vec{r}$ if the $\vec{r}$ corresponds to the angle within plus and minus 60° from the direction orienting from the external ion to the nearest-neighbor buffer ion, a longer cutoff distance than $r_{\rm L}^{\rm c}$ is used if the condition does not

meet. The non-local pseudopotentials by the external ions are assumed to be zero.

Continuation of $\rho_{\rm tot}(\vec{r})$ at the boundary $\vec{S}_{\rm bdry}$ is a principal property that should be held in the DC-RGDFT method. To realize this, the existing method [36, 37] used a soft weight-function with the embedding potential in a unique form. In the method, however, artificial density decrease of $\rho_{\rm tot}(\vec{r})$ occurs at around $\vec{S}_{\rm bdry}$ even if the unweighted density $\rho_I(\vec{r})$ is accurate at the location, as explained in a proceeding paragraph. We therefore take a different route by introducing a potential in the KS-type equation to minimize the possible difference in density at the boundary. Firstly, the density-template potential defined as

$$v_{\rm DT}(\vec{r}) = \frac{\rho_I(r) - \rho_{\rm tot}(r)}{\alpha} \tag{15}$$

is considered for domain-I with the adjustable parameter α (> 0). If $\rho_I(\vec{r}) < \rho_{\rm tot}(\vec{r})$, the $v_{\rm DT}(\vec{r})$ lowers the base of the potential in the KS-type equation and hence acts to increase $\rho_I(\vec{r})$, and vice versa. Since the $v_{\rm DT}(\vec{r})$ should work at around $\vec{S}_{\rm bdry}$ only, we secondary introduce the support function $w_{\rm DT}(\vec{r})$ to define a finite-depth layer just outside the $\vec{S}_{\rm bdry}$ as depicted in Fig. 1(c):

$$w_{\rm DT}(\vec{r}) = \frac{1}{1 + \exp[(r - d_{\rm c})/b]} \ , \tag{16}$$

where $b = d_{\rm c}/2$ and r is measured from $\vec{S}_{\rm bdry}$ toward the outside. The supported density-template potential $w_{\rm DT}(\vec{r})v_{\rm DT}(\vec{r})$ is finally added to the KS-type equation for domain-I [see, Eq. (11)]. Note that the $w_{\rm DT}(\vec{r})v_{\rm DT}(\vec{r})$ works on both real and shadow densities. We will demonstrate in the next section that the supported density-template potential is effective to stabilize the shadow density.

The $\rho_I(\vec{r})$ is assumed to decrease to zero as the $\vec{r}$ approaches to $r_{\rm max}$. Such abrupt decrease of $\rho_I(\vec{r})$ at peripheral grid points, which is an artifact of introducing the domains, may modify the eigen orbitals and energies substantially. To minimize the modification, we consider the quantum embedding effects [44] of the kinetic and exchange-correlation energies of electrons by defining the embedding potential

$$v_{\rm emb}(\vec{r}) = \frac{\delta T_{\rm s}(\rho_{\rm tot})}{\delta \rho_{\rm tot}(\vec{r})} - \frac{\delta T_{\rm s}(\rho_I)}{\delta \rho_I(\vec{r})} + \frac{\delta E_{\rm xc}(\rho_{\rm tot})}{\delta \rho_{\rm tot}(\vec{r})} - \frac{\delta E_{\rm xc}(\rho_I)}{\delta \rho_I(\vec{r})} \ , \tag{17}$$

where $T_{\rm s} = \sum_{n=1}^{N_{e,I}/2} \int d\vec{r} \phi_n^*(\vec{r})(-\nabla^2)\phi_n(\vec{r})$ and $E_{\rm xc}$ is the exchange-correlation energy. The LDA is applied to $T_{\rm s}$ and $E_{\rm xc}$. When $\rho_I(\vec{r})$ differs from $\rho_{\rm tot}(\vec{r})$,

the $v_{\rm emb}(\vec{r})$ acts to shift up or down the base of the potential to take into account the many-body quantum effects of electrons. At a high density situation with $r_s \equiv (3/4\pi\rho_{\rm tot})^{1/3}/a_{\rm B} < 3$, the Fermi degeneracy effect dominates and thereby shifts up the averaged electron energy; at a low density with $r_s > 3$, the exchange-correlation effect dominates and shifts down the averaged electron energy. Since the $v_{\rm emb}(\vec{r})$ should work only at the artificially decreasing tail of $\rho_I(\vec{r})$, the supported embedding potential defined as $[1 - w_{\rm DT}(\vec{r})]v_{\rm emb}(\vec{r})$ is added in the KS-type equation for domain-I [see, Eq. (11)].

Let us compare the present method with existing similar methods. The AODFT method uses the pre-computed AO basis set to describe the eigen orbitals. To advance the AODFT method to the DC-type, only the classical embedding effects of the Hartree and ionic Coulomb potentials are considered with soft weight functions [30, 32, 33, 34]. Hence the DC-AODFT method requires relatively thick buffer layers to obtain accurate results. As a side effect of using the AO basis set, the shadow density relating to the buffer ions fluctuates little in the DC-AODFT method. Therefore the density-template potential is not considered in the DC-AODFT method.

Difference between the existing method in Ref. [36] and the present one is clarified below. Both methods use the RGDFT method for each domain. In Ref. [36], the quantum embedding effect of the kinetic energy is considered for a domain in addition to the classical embedding effect of the Hartree and ionic Coulomb potentials, while the density-template potential is not considered. Hence the KS-type equation for domain-I in Ref. [36] contains the embedding potential

$$\overline{v}_{\rm emb}(\vec{r}) = \frac{\delta T_s(\rho_{\rm tot})}{\delta\rho_{\rm tot}(\vec{r})} - \left(\frac{\delta T_s(\rho)}{\delta\rho}\right)_{\rho=W_I(\vec{r})\rho_I(\vec{r})} \tag{18}$$

with a soft weight-function $W_I(\vec{r})$. The method ignores the shadow density and regards the real density as embedded in $\rho_{\rm tot}(\vec{r})$. The method may cause the following problem. Let us consider the case of applying the method to a homogeneous system with a soft weight-function. In the case, the $\rho_I(r)$ should be nearly equal to $\rho_{\rm tot}(r)$ at around $\vec{S}_{\rm bdry}$. Since the inequality $W_I(\vec{r})\rho_I(\vec{r}) < \rho_{\rm tot}(\vec{r})$ holds for a thick region (relating to the softness of the weight function) at around $\vec{S}_{\rm bdry}$, the embedding potential takes on positive values, i.e., $\overline{v}_{\rm emb}(\vec{r}) > 0$, in the region. It means that $\rho_I(\vec{r})$ will be suppressed artificially in the region by $\overline{v}_{\rm emb}(\vec{r})$ despite the intrinsic homogeneity of the

system, resulting in inhomogeneity of $\rho_{\rm tot}(\vec{r})$. In our formulation for the embedding potential, no such an unphysical situation is expected to occur.

In Refs. [45, 46], both density-template and embedding potentials are ignored in the KS-type equation for a domain. As in the present method, the eigen orbitals are assumed to vanish outside the spherical grid points. The radii (i.e., $\{r_{\rm max}\}$) and locations of the domains are optimized adaptively for a target system during the calculation. We will show in §3.2 that inclusion of both potentials in the KS-type equation make the calculated density and atomic forces have similar high accuracies irrespective of target systems without such an optimization procedure.

In the DC-RGDFT method we calculate the forces on atoms as follows. For an ion-i with charge number Z_i at position $\vec{R}_i$, we firstly identify the basic domain I to which the ion belongs. Using the eigen orbitals and $\rho_I(\vec{r})$ for domain-I, we then calculate the force $\vec{F}_i$ acting on atom-i based on the Hellmann-Feynmann formula [8]:

$$\begin{aligned}\vec{F}_i &= -\int d\vec{r} v_{\rm xc}(\rho_I(\vec{r})+\rho_{c,I}(\vec{r}))\frac{\partial \rho_{c,I}(\vec{r})}{\partial \vec{R}_i} - \int d\vec{r}\frac{\partial v_{{\rm L},i}(\vec{r})}{\partial \vec{R}_i}\rho_{\rm tot}(\vec{r}) \\ &- \sum_{n=1}^{N_{e,I}/2} 2\langle\phi_n|\frac{\partial v_{{\rm NL},i}(\vec{r})}{\partial \vec{R}_i}|\phi_n\rangle + \sum_{j}^{\neq i}\frac{Z_i Z_j(\vec{R}_i-\vec{R}_j)}{|\vec{R}_i-\vec{R}_j|^3}\ , \end{aligned} \tag{19}$$

where $\rho_{c,I}(\vec{r})$ is the partial core-charge density [47] of the real ions. The atomic force, $\vec{F}_i$, is explicitly independent of the weight function. We expect the combination of the density-template and embedding potentials makes the total density in the DC-RGDFT method comparable to that in the RGDFT method, resulting in high accuracy in atomic forces.

3. Accuracy and timing

3.1. Implementation of DC-RGDFT method

The KS-type equation for each domain [Eq. (11)] is treated on the real-space grid points that form a sphere. The grid size h is common to all the domains. The KS-type equations are solved simultaneously for all the domains by repeating the following SCF iteration procedure. As shown in Fig. 2, the procedure for a given set of densities $\{\rho_I(\vec{r})\}$ is composed of the following three major steps: (i) The local iteration in each domain about the orbitals

by the conjugate gradient (CG) method [8, 11] with their mutual orthonormalization. The global Fermi energy is determined. (ii) The transferring of data on the overlapping grid points between the domains with respect to the weighted densities, $\{W_I(\vec{r})\rho_I(\vec{r})\}$, and the corresponding Hartree potentials. (iii) The update of the set of densities $\{\rho_I(\vec{r})\}$ using the Pulay mixing method [48, 49].

For the step (i) we exploits the RGDFT code [13, 14, 21] that is parallelized following the spatial decomposition strategy to treat the grid points by multiple compute-nodes. The local CG iteration is repeated for about 3-5 times per orbital. It is composed of the updates of the orbitals and of their Gram-Schmidt orthonormalization all together. The pre-conditioning (or smoothing) of the gradients of the orbitals using the six nearest-neighbor grid point data (two for each direction) with the relative weight 0.1 with respect to the central point is important for numerical stability. The fourth order finite difference method that uses nine data points for each direction is adopted to evaluate the second derivative term; the possible error is order-h^{10}. Detail of the local CG iteration has been explained [13, 14, 21, 22, 23].

As for the step (ii), the communicator (or the group of compute-nodes) for inter-domain communication is prepared for the MPI standard [50], in addition to the communicator for each domain for intra-domain communication. For a given cutoff depth $d_{\rm c}$, the buffer ions are selected and then the maximum radius $r_{\rm max}$ for the spherical grid points is determined for each domain. The overlaps of the spheres are pre-computed and saved for transferring of data on the overlapping grid points between the domains. To compute the Hartree potential relating to $\rho_{\rm tot}(\vec{r})$, the Poisson equation for the weighted density $W_I(\vec{r})\rho_I(\vec{r})$ is solved for each domain. If a grid point of a domain overlaps to the point of a neighboring domain, the Hartree potential on the point obtained by the Poisson solution for the domain is transferred to the overlapping domain. To the non-overlapping (or far) domains, the multipole data (up to the 8th order in the spherical harmonics) [51, 52] of the weighted density are transferred instead of the Hartree potentials on the grid points. The total Hartree potential is thereby constructed by summing those contributions in each domain.

In the step (iii), the set of densities $\{\rho_I(\vec{r})\}$ is updated all together by the Pulay method [48, 49]. The maximum of ten previous sets are used to get the updated densities. For the next iteration, the eigen orbitals relating to the updated density are evaluated in the subspace spanned by the orbitals obtained at the last iteration. Thereafter the local iteration using the updated

potentials in the KS-type equations repeats. Such a SCF iteration continues for about 20-40 times until convergence that is judged using the residuals for orbitals or the change of total energy. If the residuals are not sufficiently small, we have the option to fix the $\{N_{e,I}\}$ and the Hartree potential due to the other domains to the averaged values in each domain, and to perform additional several times iterations until sufficiently small residuals are obtained in each domain.

3.2. Accuracy tests of DC-RGDFT method

To test the accuracy of the DC-RGDFT method for various materials with different electronic characters, we consider three charge-neutral systems: semiconductor Si, metallic Al, and ceramic alumina. All the three systems, rectangular in shape, are placed in vacuum. In the case of the Si, the dimensions are $(L_x, L_y, L_z) = (14.8\ \text{Å}, 9.5\ \text{Å}, 9.5\ \text{Å})$ and the total of 96 ions are arranged in the diamond crystalline structure. In the case of the Al, $(L_x, L_y, L_z) = (15.2\ \text{Å}, 10.1\ \text{Å}, 6.0\ \text{Å})$, the total of 96 ions in the fcc structure. In the case of the alumina, $(L_x, L_y, L_z) = (12.5\ \text{Å}, 8.1\ \text{Å}, 4.2\ \text{Å})$, the total of 60 ions in the α-Al_2O_3 structure. As shown in Fig. 3, two basic domains with equal size are set for each system; the boundary surface $\vec{S}_{\text{bdry}}$ is located at $L_x/2$. The cutoff depth for the buffer ions is $d_{\text{c}} = \{5.0\ a_{\text{B}}, 7.0\ a_{\text{B}}, 9.0\ a_{\text{B}}\}$ to see the dependence of the accuracy in atomic force on d_{c}. In the case of the Si, the numbers of buffer ions are 16, 24, and 32 for $d_{\text{c}} = 5.0\ a_{\text{B}}$, $7.0\ a_{\text{B}}$, and $9.0\ a_{\text{B}}$, respectively; 12, 24, and 36, in the case of the Al; 12, 18, and 22, in the case of the alumina. The grid size $h = 0.55\ a_{\text{B}}$. For the O ions only, a finer grid of $h/3$ is used to describe the local and non-local pseudopotentials. The parameter α for the density-template potential in Eq. (15) is determined heuristically as $\alpha = 0.033$ in the atomic unit for all three systems. We note that the calculated density and forces are not sensitive to the value of α. The cutoff radii for the Coulomb potentials of the external ions [see, Fig. 1(b)] are set also as: $r_{\text{L}}^{\text{c}} = 1.4\ a_{\text{B}}$, $1.8\ a_{\text{B}}$, and $1.5\ a_{\text{B}}$, for Si, Al, and O ions, respectively.

Figure 4 shows the $\rho_0(\vec{r})$ of domain-0 in the Si system for $d_{\text{c}} = 5.0\ a_{\text{B}}$. The 3D isosurface at $0.07\ a_{\text{B}}^{-3}$ is shown in Fig. 4(a); the 2D intensity map on $L_z/2$, in Fig. 4(b). Besides, to see the effects of the density-template and embedding potentials separately, the $\rho_0(\vec{r})$ if only the density-template potential is used is depicted in Figs. 4(c) and (d); the $\rho_0(\vec{r})$, if only the embedding potential, in Figs. 4(e) and (f). The $\rho_0(\vec{r})$ in basic domain-0 appears to be unaffected by changing the potential setting. On the other hand, the $\rho_0(\vec{r})$ outside

basic domain-0 (i.e., the shadow density) differs substantially between the potential settings. If only the density-template potential is used, the shadow density extends much to the x-direction (i.e., toward the other domain) as seen in Figs. 4(c) and (d). This is expected because the density-template potential, which works at around the boundary $\vec{S}_{\rm bdry}$ in the buffer region, acts to make $\rho_0(\vec{r})$ close to $\rho_{\rm tot}(\vec{r})$ at the region. As seen in Figs. 4(e) and (f), the embedding potential only is not sufficient to stabilize the shadow density of $\rho_0(\vec{r})$. Though the partial shadow-density $[1 - W_0(\vec{r})]|\phi_i(\vec{r})|^2$ of eigen orbital-i, which exists outside basic domain-0 near the boundary $\vec{S}_{\rm bdry}$, gives no contribution to $\rho_{\rm tot}(\vec{r})$, variation of the partial shadow-density affects not only the $\phi_i(\vec{r})$ itself but also all the other eigen orbitals in domain-0 through the orthogonality relation. Stability of the shadow density is essential for both fast convergence in the SCF iteration and accurate atomic forces.

Similar analyses about the calculated $\rho_0(\vec{r})$ are performed for both Al and alumina systems with $d_{\rm c} = 5.0\ a_{\rm B}$ as depicted in Figs. 5 and 6, respectively. For the Al system, the 3D isosurface at $0.02\ a_{\rm B}^{-3}$ is shown; the 3D isosurface at $0.04\ a_{\rm B}^{-3}$ for the alumina system. As has been found for the Si system, the embedding potential alone cannot produce the shadow density properly for both Al and alumina systems. Substantial spatial fluctuation of the shadow density occurs if the embedding potential alone is used for the Al system, while abrupt decrease of the shadow density at around the distance of $d_{\rm c}$ from the $\vec{S}_{\rm bdry}$ is seen for the alumina system. In both Al and alumina systems, the density-template potential acts to extend $\rho_0(\vec{r})$ to the x-direction in similar ways to the case of the Si system.

The total density calculated as $\rho_{\rm tot}(\vec{r}) = W_0(\vec{r})\rho_0(\vec{r}) + W_1(\vec{r})\rho_1(\vec{r})$ is plotted in Figs. 7(a) and (b) for the Si system, in Figs. 7(c) and (d) for the Al system, and in Figs. 7(e) and (f) for the alumina system. In Figs. 7(a), (c), and (e), the 3D isosurfaces at the same density values as in Figs. 4–6 are plotted with the ions drawn by the spheres. Figures 7(b), (d), and (f) are the corresponding 2D mappings of density on the $L_z/2$ surfaces. The $\rho_{\rm tot}(\vec{r})$ agrees accurately with that obtained separately by the RGDFT method; the maximum deviation in density is smaller than $10^{-4} a_{\rm B}^{-3}$.

We proceed to analyze the accuracy of atomic forces in the DC-RGDFT method. We define the deviations of the forces $\{\delta F_i \equiv |\vec{F}_i - \vec{F}_{{\rm ref},i}|\}$ from the reference values $\{\vec{F}_{{\rm ref},i}\}$ calculated by the RGDFT method with the same grid size h. Table I lists the maximum and average of $\{\delta F_i\}$ over all the atoms in the system for various $d_{\rm c} = 5.0\ a_{\rm B}$, $7.0\ a_{\rm B}$, and $9.0\ a_{\rm B}$; the Si, Al, and alumina

systems are considered. For the Si and alumina systems, both maximum and average of $\{\delta F_i\}$ decrease significantly as the d_c increases. Less significant decreasing behavior relating to the increase of d_c is seen for the Al system. We guess that it is a result of relatively long nature [53, 54] of the density correlation in a metallic system as Al. For all the three systems the maximum of $\{\delta F_i\}$ is equal or smaller than 0.01 a.u. (1 a.u. of force ≈ 51.4 eV/Å) for $d_c = 5.0\ a_B$, which corresponds to a virtual shift of an atom by as small as 0.01–0.02 Å. We may state that the setting of $d_c = 5.0\ a_B$ gives sufficient accuracy in atomic forces for dynamics simulations of all three systems.

We demonstrate the importance of combining the density-template and embedding potentials to realize accurate atomic forces in the DC-RGDFT method. The maxima of $\{\delta F_i\}$ for the (Si, Al, alumina) systems calculated for $d_c = 5.0\ a_B$ with neither the density-template nor the embedding potential are (0.060 a.u., 0.0071 a.u., 0.115 a.u.); (0.242 a.u., 0.025 a.u., 0.32 a.u.) if only the embedding potential is used; (0.031 a.u., 0.0045 a.u., 0.019 a.u.) if only the density-template potential is used. Since the maxima of $\{\delta F_i\}$ calculated with density-template and embedding potentials are (0.0109 a.u., 0.0042 a.u., 0.0094 a.u.) as shown in Table I, it is clear that the combination of both potentials make the maximum of $\{\delta F_i\}$ small for all three systems.

If we use the existing method in Ref. [36] with the same settings of $d_c = 5.0\ a_B$ and the stepwise weight-functions $\{W_I(\vec{r})\}$, the maximum and average of $\{\delta F_i\}$ are respectively, 0.34 a.u. and 0.025 a.u. for the Si system; 0.098 a.u. and 0.026 a.u. for the Al system; 0.41 a.u. and 0.033 a.u. for the alumina system. Relatively large errors in atomic forces result.

3.3. Timing tests of DC-RGDFT code on parallel machines

In this subsection, we perform timing tests of the DC-RGDFT code using two parallel machines with different architectures: one is TSUBAME2.0 at Tokyo Institute of Technology (Intel Xeon X5670 2.93GHz, InfiniBand QDR) and the other is Fujitsu FX1 at Nagoya University (SPARC64 VII 2.5GHz, InfiniBand DDR). For the target systems, we consider charge-neutral Al crystalline systems in vacuum. The numbers of Al ions $N_{\rm ion}$ are 48, 384, 1296, 3072, 3840, and 6000, which are treated by the DC-RGDFT method with $N_{\rm d} \equiv N_{{\rm d},x} N_{{\rm d},y} N_{{\rm d},z}$ domains arranged in 3D as $(N_{{\rm d},x}, N_{{\rm d},y}, N_{{\rm d},z}) = (1,1,1)$, $(2,2,2)$, $(3,3,3)$, $(4,4,4)$, $(5,4,4)$, and $(5,5,5)$, respectively. Each basic domain is a collection of the same numbers $(N_{{\rm cell},x}, N_{{\rm cell},y}, N_{{\rm cell},z}) = (3,2,2)$ of cells of the fcc unit composed of four ions, which therefore contains 48 real ions with varying number of buffer ions depending on both location of the

domain and $N_{\rm d}$. The cutoff depth for the buffer ions is set as $d_{\rm c} = 5.0\ a_{\rm B}$. Each domain that contains the real and buffer ions is treated with twelve compute-nodes (or CPU cores) of a parallel machine by spatially dividing the spherical grid points into three, two, and two in the x, y, and z directions, respectively. Therefore the computation power increases linearly with $N_{\rm ion}$. The number of the SCF iterations is fixed to 25. The vacuum radius, which is added to the minimum radius of the sphere that encloses the real and buffer ions, is set to 6.0 $a_{\rm B}$. The grid size $h = 0.85\ a_{\rm B}$ because the error in atomic force is order 0.01 a.u. Five runs with $N_{\rm ion} = 48$, 384, 1296, 3072, and 6000 are performed on TSUBAME2.0, while five runs with $N_{\rm ion} = 48$, 384, 1296, 3072, and 3840 on FX1.

Figure 8(a) shows the results of the wall-clock time for TSUBAME2.0 required to calculate the eigen orbitals and atomic forces starting with the random number orbitals, for various cases of $N_{\rm ion}$. For references, the times required when the RGDFT method is used with the same number of compute-nodes for the same target systems are plotted. We find in Fig. 8(a) that the time for the DC-RGDFT method increases substantially up to $N_{\rm d} = 3^3$. It is because the maximum number of the buffer ions for the domains, which corresponds to that for the central domain in the 3D arrangement of domains, increases up to the case of $N_{\rm d} = 3^3$ and becomes constant for $N_{\rm d} = 4^3$ and 5^3. The time saturates for $N_{\rm d} \geq 4^3$, relating to the order-N scaling nature of the DC-RGDFT method. It is also clear in Fig. 8(a) that the DC-RGDFT method is much faster the RGDFT method as expected.

Let us consider about the inter-domain communication time that emerges when the RGDFT method is advanced to the DC-type. Dominant contribution of the inter-domain communication is the transferring of both weighted density and corresponding Hartree potential on the overlapping grid points of two spheres with radii $\{r_{\rm max}\}$. The $r_{\rm max} = 21.2$–$25.5\ a_{\rm B}$ in the present systems. The domain centers form a deformed rectangular lattice with the x, y, and z spacings of 18.7–23.0 $a_{\rm B}$, 11.1–15.3 $a_{\rm B}$, and 11.1–15.3 $a_{\rm B}$, respectively. Therefore the inter-domain communication about the grid point data grows substantially until $(N_{{\rm d},x}, N_{{\rm d},y}, N_{{\rm d},z}) = (5, 5, 5)$. In the case of $(N_{{\rm d},x}, N_{{\rm d},y}, N_{{\rm d},z}) = (5, 5, 5)$ the central domain, for instance, communicates with 100 domains, while the edge domain with 33 domains. Such a inter-domain communication is performed in parallel between the nodes. The amount of inter-domain communication data averaged over the nodes is 14.1 MB for $(N_{{\rm d},x}, N_{{\rm d},y}, N_{{\rm d},z}) = (2, 2, 2)$ during the 25 times SCF iterations, 35.5 MB for $(N_{{\rm d},x}, N_{{\rm d},y}, N_{{\rm d},z}) = (3, 3, 3)$, 67.8 MB for $(N_{{\rm d},x}, N_{{\rm d},y}, N_{{\rm d},z}) =$

$(4, 4, 4)$, and 72.7 MB for $(N_{\mathrm{d},x}, N_{\mathrm{d},y}, N_{\mathrm{d},z}) = (5, 5, 5)$. Figure 8(b) shows the inter-domain communication time as well as the total computation time for FX1. The total computation time for FX1 is about twice of that for TSUBAME2.0. We find in Fig. 8(b) that the inter-domain communication time averaged over the nodes is less than 1% of the total computation time in all cases for FX1. Similar small fraction of the inter-domain communication time is expected for TSUBAME2.0 also though we have not measured it in the present tests.

4. Summary and concluding remarks

In the present paper, we have developed the DC-RGDFT method for various materials by advancing the existing formulation in Ref. [36]. In the Kohn-Sham-type equation for a domain, we have introduced the density-template potential for the density continuity with the simple stepwise weight-functions. We have also introduced the embedding potential to take into account all the quantum correlation effects with other domains in addition to the classical embedding effects of electronic and ionic Coulomb potentials. We have thereby obtained reasonable accuracies in atomic forces for various materials including the semiconductor Si, the metallic Al, and the ceramic alumina with relatively small numbers of buffer ions. The timing tests of the DC-RGDFT code on parallel machines have demonstrated the order-N scaling of it with little communication time between the domains.

As stated in §1, we plan to use the DC-RGDFT method as the QM method in the hybrid QM-CL simulation for various problems. One of the problems is the Li transport in the Li-ion battery. In the Li-ion battery, there forms the solid-electrolyte interphase (SEI) [55] on both negative and positive electrodes by electrochemical reactions. Graphite has been used as the negative electrode. The SEI is considered to help stabilize the electrodes, while the Li transport through the SEI is a principal process that determines the performance of the battery. Understanding the microscopic structure of the SEI formed on the graphite and the Li transport through that, is crucial to advance the Li-ion battery. One of the model molecules that form the SEI on the graphite is the dilithium ethylene dicarbonate (Li_2EDC) [56]. We have started to apply the DC-RGDFT method to simulate the Li_2EDC-based SEI system at around the graphite. Figure 9(a) depicts the QM region composed of C, H, O, and Li in the hybrid QM-CL simulation of such a system, which is treated with four domains in the DC-RGDFT method. Figure 9(b) shows the

isosurfaces at 0.03 a_{B}^{-3}, 0.1 a_{B}^{-3}, and 0.3 a_{B}^{-3} of the calculated total density. No density discontinuity is observed at the boundary. The calculated density agrees quite well with that obtained with the RGDFT method. The atomic forces, whose accuracy is crucial for the dynamics, compare well with that in the RGDFT method.

Further advancement of the DC-RGDFT code is in progress. It is desirable to obtain the total energy in the DC-RGDFT method to calculate, for instance, the barrier energy of a chemical reaction process. To obtain accurate total energy, we need to minimize the artificial effects from the buffer region on the total energy. Note that the total energy in the DC-RGDFT method cannot be decomposed explicitly to the contributions of atomic pairs unlike in the AO-based approach. Critical examination of the accuracy of the total energy is in progress. It is also often desirable to obtain the eigen orbitals that may spread over the total system at around the Fermi level when one tries to investigate the mechanism of a chemical reaction. A post calculation will be added to obtain the global eigen orbitals for the calculated total density without performing the SCF iteration.

Acknowledgements

This research was supported by JST Core Research for Evolutional Science and Technology (CREST), JSPS KAKENHI (23310074), and MEXT Strategic Programs for Innovative Research (SPIRE) and Computational Materials Science Initiative (CMSI) of Japan. The benchmark tests were carried out on TSUBAME2.0 at Global Scientific Information and Computing Center of Tokyo Institute of Technology supported by the MEXT Open Advanced Research Facilities Initiative, and on Fujitsu FX1 at Information Technology Center of Nagoya University. The density plots were made using the visualization package VESTA [57].

References

[1] P. Hohenberg, W. Kohn, Phys. Rev. 136 (1964) B864.

[2] W. Kohn, L. Sham, Phys. Rev. 140 (1965) A1133.

[3] R.G. Parr, W. Yang, Density-Functional Theory of Atoms and Molecules (Oxford Sci. Pub., New York, 1994).

[4] J.H. Fendler, Ed., Nanoparticles and Nanostructured Films (Wiley-VCH, New York, 1998).

[5] R. Ghodssi, P. Lin, MEMS Materials and Processes Handbook (Springer, Berlin, 2011).

[6] A. Nakano, R.K. Kalia, P. Vashishta, Sci. Programming 10 (2002) 263.

[7] A. Nakano, M.E. Bachlechner, P. Branicio, et al., IEEE Trans. Electron Devices 47 (2000) 1804.

[8] M.C. Payne, M.P. Teter, D.C. Allan, et al., Rev. Mod. Phys. 64 (1992) 1045.

[9] G. Kresse, J. Furthmüller, Phys. Rev. B 54 (1996) 11169.

[10] E. Bichoutskaia, Ed., Computational Nanoscience, RSC Pub., Cambridge, 2011.

[11] e.g., W.H. Press, S.A. Teukolsky, W.T. Vetterlin, et al., Numerical Recipies in Fotran77, 2nd Ed. (Cambridge Univ. Press, New York, 1992).

[12] e.g., N. Bernstein, J.R. Kermode, G. Csányi, Rep. Prog. Phys. 72 (2009) 026501.

[13] S. Ogata, E. Lidorikis, F. Shimojo, et al., Comput. Phys. Comm. 138 (2001) 143.

[14] S. Ogata, F. Shimojo, R.K. Kalia, et al., Comput. Phys. Comm. 149 (2002) 30.

[15] S. Ogata, Phys. Rev. B 72 (2005) 045348.

[16] J.R. Chelikowsky, N. Troullier, Y. Saad, Phys. Rev. Lett. 72 (1994) 1240.

[17] J.R. CHelikowsky, N. Troullier, K. Wu, et al., Phys. Rev. B 50 (1994) 11355.

[18] E.L. Briggs, D.J. Sullivan, J. Bernholc, Phys. Rev. B 52 (1995) R5471.

[19] E.L. Briggs, D.J. Sullivan, J. Bernholc, Phys. Rev. B 54 (1996) 14362.

[20] I.-H. Lee, Y.-H. Kim, R.M. Matrin, Phys. Rev. B 61 (2000) 4397.

[21] F. Shimojo, T.J. Campbell, R.K. Kalia, et al., Future Gener. Comput. Syst. 17 (2000) 279.

[22] U.V. Waghmare, H. Kim, I.J. Park, et al., Comput. Phys. Comm. 137 (2001) 341.

[23] J.-I. Iwata, D. Takahashi, A. Oshiyama, et al., J. Comput. Phys. 229 (2010) 2339.

[24] T. Kouno, S. Ogata, J. Phys. Soc. Jpn. 77 (2008) 054708.

[25] N. Ohba, S. Ogata, T. Tamura, et al., Comput. Model. in Eng. & Sci. 75 (2011) 247.

[26] S. Ogata, Y. Abe, N. Ohba, et al., J. Appl. Phys. 108 (2010) 064313.

[27] S. Ogata, F. Shimojo, A. Nakano, et al., J. Appl. Phys. 95 (2004) 5316.

[28] M.W. Schmidt, K.K. Baldridge, J.A. Boatz, et al., J. Comput. Chem. 14 (1993) 1347; GAMESS

[29] Y. Shao, L. Fusti-Molnar, Y. Jung, et al., Phys. Chem. Chem. Phys. 8 (2006) 3172; Q-CHEM

[30] W. Yang, Phys. Rev. Lett. 66 (1991) 1438.

[31] W. Yang, Phys. Rev. A 44 (1991) 7823.

[32] Z. Zhou, Chem. Phys. Lett. 203 (1993) 396.

[33] W. Yang, T.-S. Lee, J. Chem. Phys. 103 (1995) 5674.

[34] T. Zhu, W. Pan, Phys. Rev. B 53 (1996) 12713.

[35] T. Ozaki, Phys. Rev. B 74 (2006) 245101.

[36] F. Shimojo, R.K. Kalia, A. Nakano, et al., Comput. Phys. Comm. 167 (2005) 151.

[37] F. Shimojo, R.K. Kalia, A. Nakano, et al., Phys. Rev. B 77 (2008) 085103.

[38] F. Shimojo, A. Nakano, R.K. Kalia, et al., Appl. Phys. Lett. 95 (2009) 043114.

[39] L. Kleinman, D.M. Bylander, Phys. Rev. Lett. 48 (1982) 1425.

[40] N. Troullier, J.L. Martins, Phys. Rev. B 43 (1991) 1993.

[41] J.P. Perdew, A. Zunger, Phys. Rev. B 23 (1981) 5048.

[42] D.M. Bylander, L. Kleinman, S. Lee, Phys. Rev. B 42 (1990) 1394.

[43] T. Ono, K. Hirose, Phys. Rev. Lett. 82 (1999) 5016.

[44] N. Govind, Y.A. Wan, E.A. Carter, J. Chem. Phys. 110 (1999) 7677.

[45] J.-L. Fattebert, F. Gygi, Comput. Phys. Comm. 162 (2004) 24.

[46] J.-L. Fattebert, J. Phys. Condens.Matter 20 (2008) 294210.

[47] S.G. Louie, S. Froyen, M.L. Cohen, Phys. Rev. B 26 (1982) 1738.

[48] P. Pulay, Chem. Phys. Lett. 73 (1980) 393.

[49] P. Pulay, J. Comp. Chem. 3 (1982) 556.

[50] W. Gropp, E. Lusk, A. Skkjellum, Using MPI: Portable Parallel Programming with the Message-Passing Interface (MIT Press, Boston, 1994).

[51] S. Ogata, T.J. Campbell, R.K. Kalia, et al., Comput. Phys. Comm. 153 (2003) 445.

[52] L. Greengard, V. Rokhlin, J. Comput. Phys. 74 (1987) 325.

[53] W. Kohn, Phys. Rev. B 115 (1959) 809.

[54] W. Kohn, Phys. Rev. Lett. 76 (1996) 3168.

[55] e.g., K. Xu, Chem. Rev. 104 (2004) 4303.

[56] O. Borodin, G.D. Smith, P. Fan, J. Phys. Chem. B 110 (2006) 22773.

[57] K. Momma, F. Izumi, J. Appl. Crystallogr. 41 (2008) 653.

Table 1: The maximum and average of the deviations of the atomic forces $\{\delta F_i = |\vec{F}_i - \vec{F}_{\mathrm{ref},i}|\}$ obtained by the DC-RGDFT method for various systems depicted in Fig. 3 with various cutoff depths d_{c}'s for the buffer ions. The reference values $\{\vec{F}_{\mathrm{ref},i}\}$ are calculated by the RGDFT method. ($1a_{\mathrm{B}} \approx 0.529$ Å, 1 a.u. of force ≈ 51.4 eV/Å).

system	d_{c} (a_{B})	$(\delta F)_{\mathrm{max}}$ (a.u.)	$(\delta F)_{\mathrm{ave}}$ (a.u.)
Si_{96}	5.0	0.0109	0.0018
Si_{96}	7.0	0.0034	0.0009
Si_{96}	9.0	0.0028	0.0009
Al_{96}	5.0	0.0042	0.0023
Al_{96}	7.0	0.0040	0.0022
Al_{96}	9.0	0.0040	0.0021
$Al_{24}O_{36}$	5.0	0.0094	0.0022
$Al_{24}O_{36}$	7.0	0.0037	0.0011
$Al_{24}O_{36}$	9.0	0.0037	0.0008

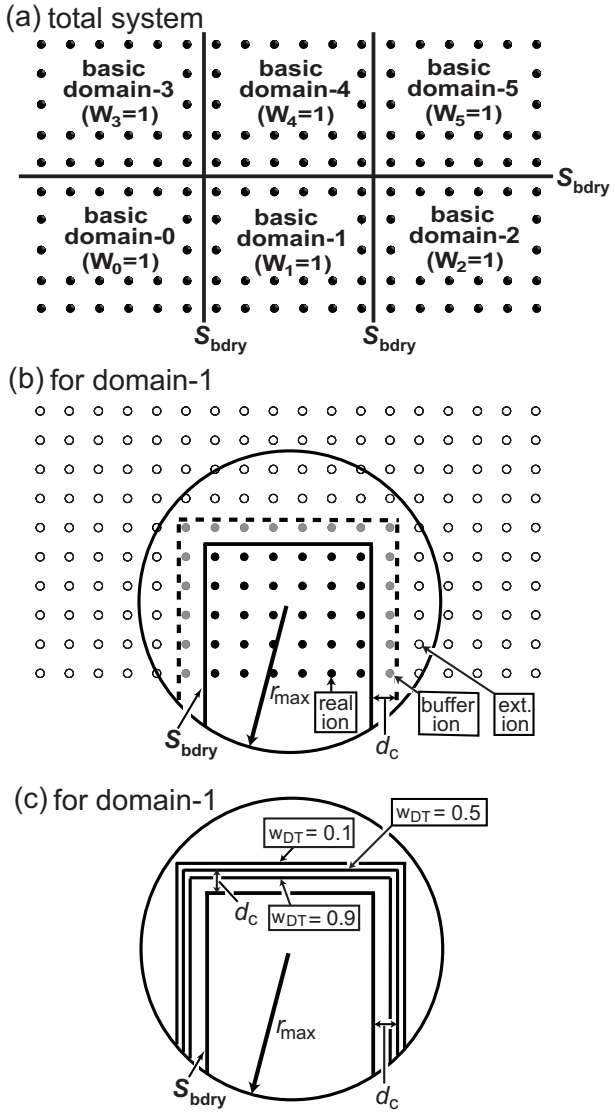

Figure 1: (a) Schematic 2D view of the division of a target system into basic domains in the DC-RGDFT method. The dots represent the ions. The boundary surfaces $\vec{S}_{\rm bdry}$ are indicated with the lines. (b) Identification of all the ions as either the real, buffer, or external ones for domain-1 in (a). The cutoff depth $d_{\rm c}$ and the maximum radius $r_{\rm max}$ of the spherical grid points for domain-1 are depicted with the boundary surfaces. (c) Contour map of the support function, $w_{\rm DT}(\vec{r})$, for domain-1 in (b).

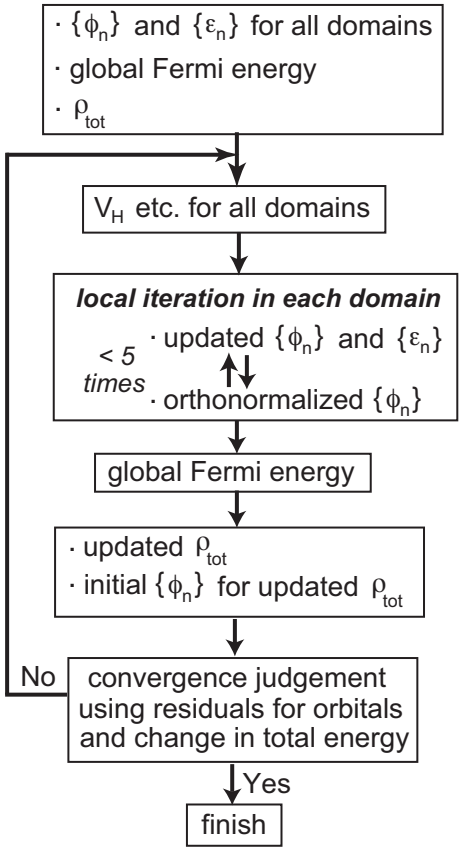

Figure 2: Brief flowchart of the SCF iteration procedure in the DC-RGDFT method. The $\{\phi_n\}$ and $\{\epsilon_n\}$ are the eigen orbitals and energies for the KS-type equations, respectively. The $\rho_{\rm tot}$ is the total density of electrons.

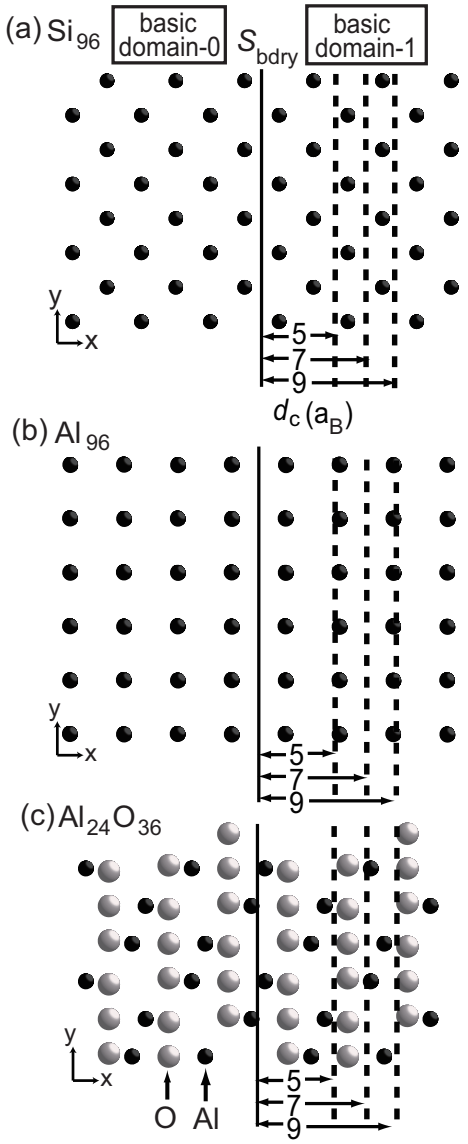

Figure 3: The x-y views of the test systems to be treated by the DC-RGDFT method. Two basic domains (0 and 1) are depicted. Various cutoff depths $d_{\rm c} = \{5.0\ a_{\rm B}, 7.0\ a_{\rm B}, 9.0\ a_{\rm B}\}$ for the buffer ions are depicted for domain-0. ($1a_{\rm B} \approx 0.529$ Å). (a) The crystalline Si_{96} system, (b) the crystalline Al_{96} system, and (c) the α-alumina $Al_{24}O_{36}$ system.

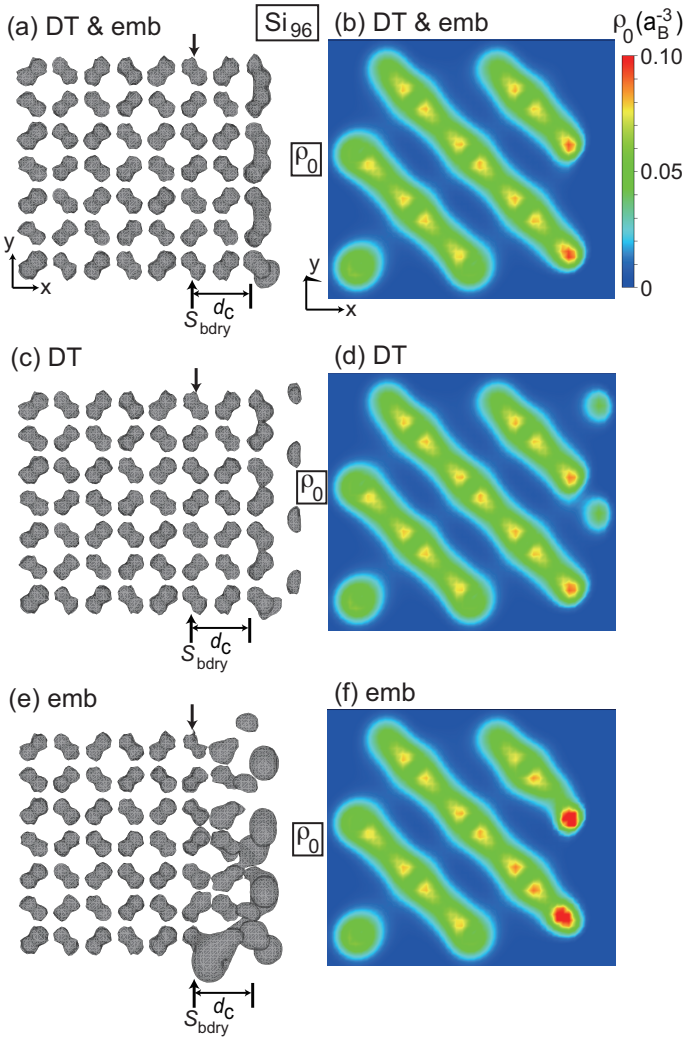

Figure 4: The x-y views of $\rho_0(\vec{r})$ for domain-0 of the Si_{96} system in Fig. 3 calculated by the DC-RGDFT method. The $d_c = 5.0\ a_B$. The grid size $h = 0.55\ a_B$. ($1a_B \approx 0.529$ Å). The (a) and (b) relate to the present formulation with both density-template and embedding potentials; (c) and (d), with the density-template potential only; (e) and (f), with the embedding potential only. The isosurfaces at $\rho_0(\vec{r}) = 0.07\ a_B^{-3}$ are plotted in (a), (c), and (e). The (b), (d) and (f) depict the 2D intensity maps on the middle surfaces perpendicular to the z-direction.

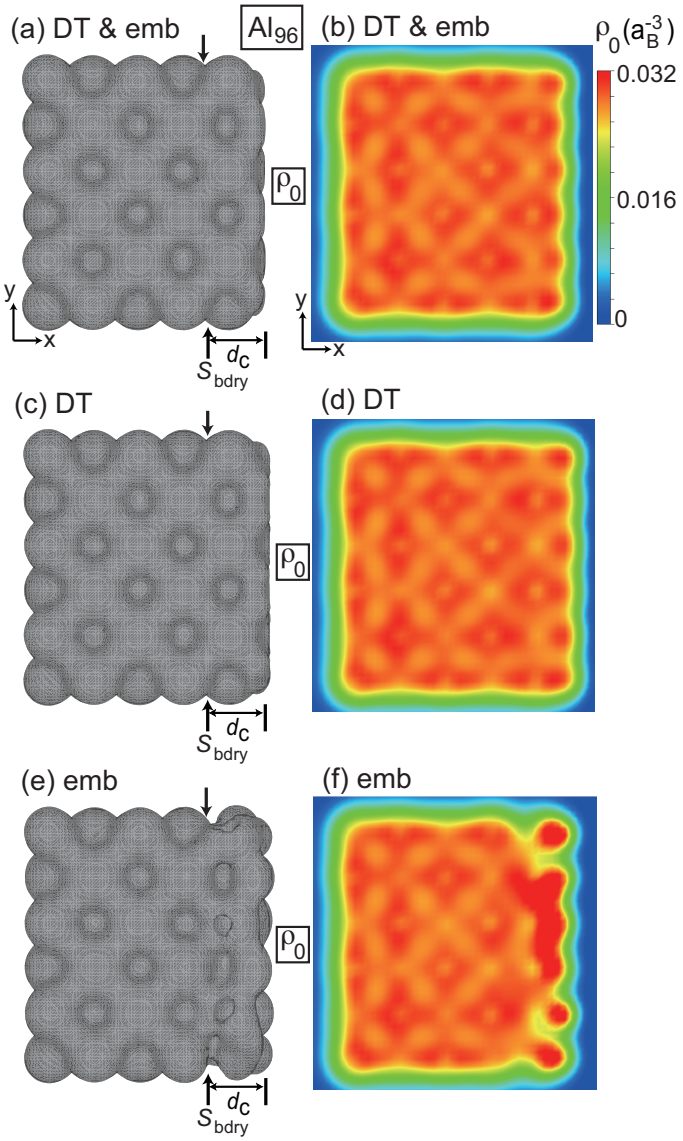

Figure 5: The same as Fig. 4, but for the Al_{96} system with the isosurfaces at $\rho_0(\vec{r}) = 0.02\ a_B^{-3}$.

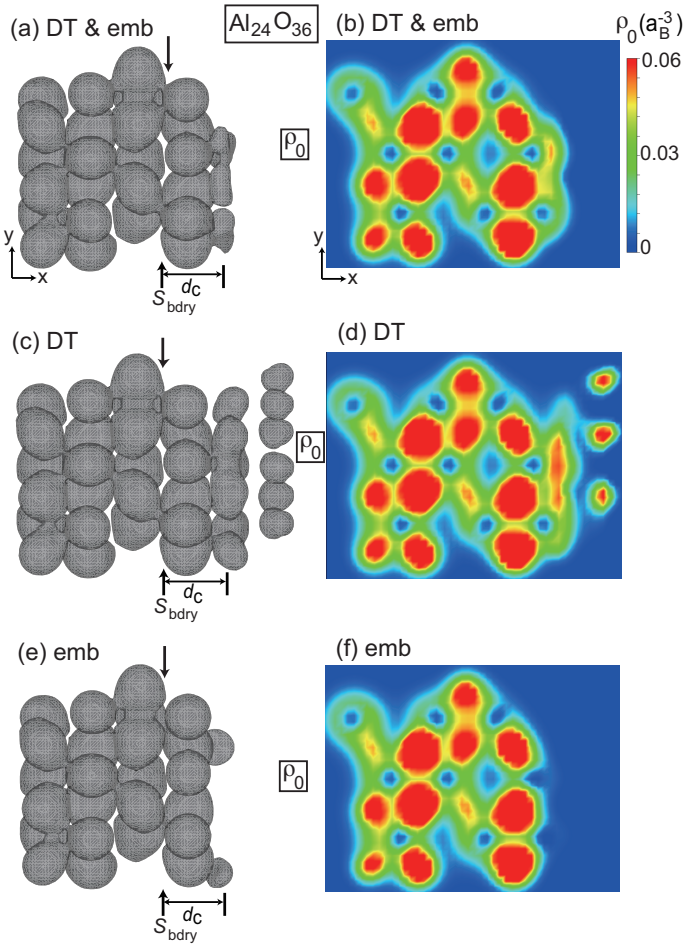

Figure 6: The same as Fig. 4, but for the $Al_{24}O_{36}$ system with the isosurfaces at $\rho_0(\vec{r}) = 0.04\ a_B^{-3}$.

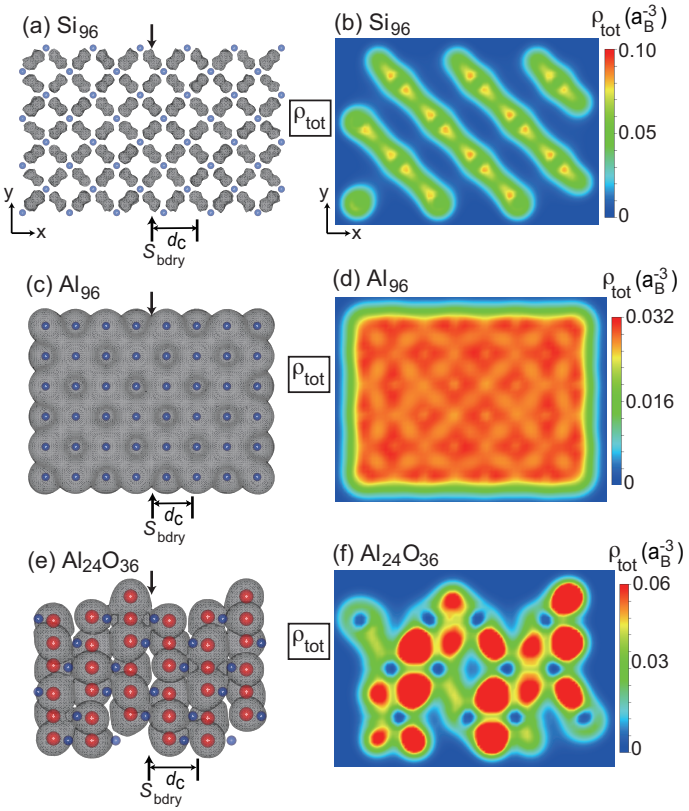

Figure 7: The x-y views of $\rho_{\rm tot}(\vec{r})$ calculated with two domains by the DC-RGDFT method. The $d_{\rm c}$ = 5.0 $a_{\rm B}$. The grid size h = 0.55 $a_{\rm B}$. ($1a_{\rm B} \approx 0.529$ Å). The (a) and (b) relate to the Si_{96} system in Fig. 3; (c) and (d), to the Al_{96} system; (e) and (f), to the $Al_{24}O_{36}$ system. The isosurfaces are drawn at $\rho_0(\vec{r}) = 0.07\ a_{\rm B}^{-3}$ with blue dots for the Si ions in (a), at 0.02 $a_{\rm B}^{-3}$ with blue dots for the Al ions in (c), and at 0.02 $a_{\rm B}^{-3}$ with blue (red) dots for the Al (O) ions in (e). The (b), (d) and (f) depict the 2D intensity maps on the middle surfaces perpendicular to the z-direction.

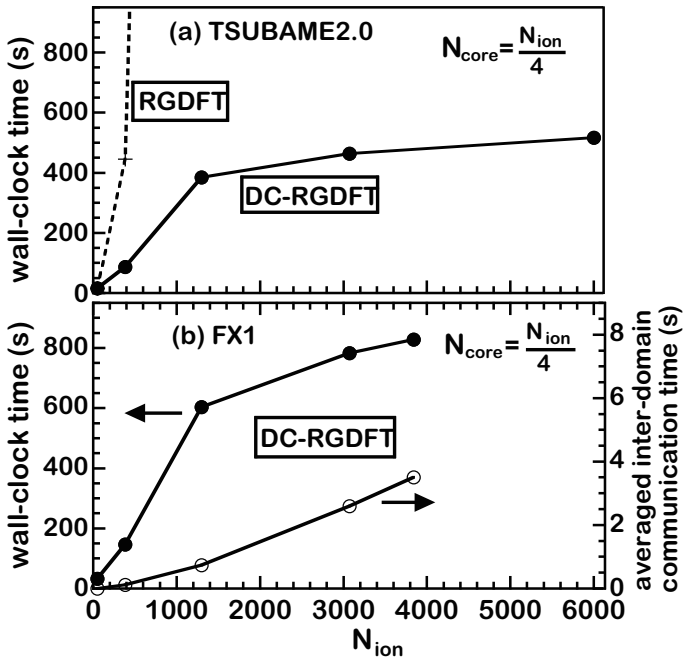

Figure 8: The wall-clock times to calculate the atomic forces of the charge-neutral crystalline Al systems in vacuum composed of $N_{\rm ion}$ Al ions and electrons by the DC-RGDFT method using $N_{\rm core}$ CPU-cores of either (a) TSUBAME2.0 or (b) Fujitsu FX1. The grid size $h = 0.85\ a_{\rm B}$. ($1a_{\rm B} \approx 0.529$ Å). The number of SCF iteration is fixed to 25. A domain contains 48 *real* ions and a varying number of *buffer* ions, which is treated with 12 CPU-cores. The inter-domain communication times averaged over the CPU-cores are plotted also in (b). For references, the corresponding results for the RGDFT method are plotted by the dashed curve in (a).

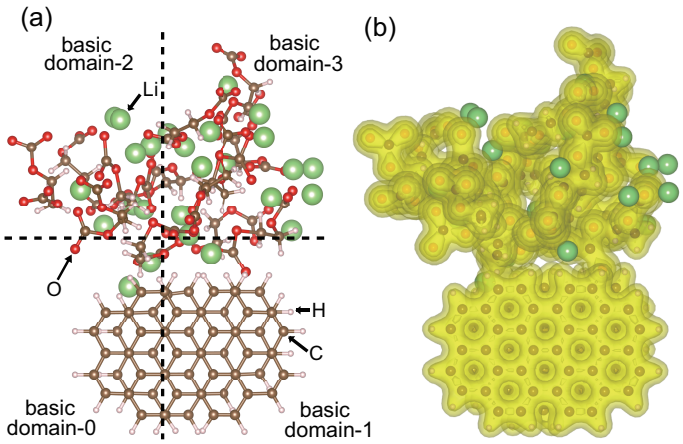

Figure 9: (a) A typical QM region selected in the hybrid QM-CL simulation of the solid-electrolyte interphase (SEI) of the graphite (negative) electrode of the Li-ion battery. The SEI is made of a model molecule, the dilithium ethylene dicarbonate. The QM region is treated with four domains by the DC-RGDFT method. (b) The isosurfaces at 0.03 a_{B}^{-3}, 0.1 a_{B}^{-3}, and 0.3 a_{B}^{-3} of the total density of the system in (a) calculated by the DC-RGDFT method. ($1a_{\mathrm{B}} \approx 0.529$ Å).